

# UNIVERSITÀ DEGLI STUDI DI PADOVA

Dipartimento di Fisica e Astronomia “Galileo Galilei”

Corso di Laurea in Fisica

Tesi di Laurea

**Newtonian chirps in a Gaussian noise background: a  
simulation study of gravitational wave signals.**

**Relatore**

**Prof. Jean-Pierre Zendri**

**Laureanda**

**Giulia Doda**

**Correlatore**

**Prof. Edoardo Milotti**

**Anno Accademico 2022/2023**



---

# Abstract

Matched filters are used in gravitational wave detection due to their optimality properties in the case of Gaussian noise. This thesis presents a simulation-based study that analyzes the performance of the match function between known gravitational wave signals, synthesized from the Newtonian coalescence model of compact binary systems, and the signals themselves injected into a noise background as the Signal-to-Noise Ratio varies. The aim is to observe and measure the dependence of the match function as a function of the Signal-to-Noise Ratio, which shows how the efficiency of this analysis method changes in different noise backgrounds. This simulation will provide a better understanding of gravitational wave detection efficiency in the LIGO-Virgo-Kagra interferometers.

---

I filtri ottimali (matched filters) vengono utilizzati nella ricerca di segnali di onde gravitazionali grazie alle loro proprietà di ottimalità nel caso di rumore Gaussiano. In questa tesi viene svolto uno studio basato su simulazioni in cui si analizza l'andamento della funzione di match fra i segnali sintetizzati a partire dal modello Newtoniano delle coalescenze di sistemi binari compatti e i segnali stessi iniettati in un fondo di rumore al variare del rapporto segnale-rumore. Lo scopo è quello di osservare e misurare la dipendenza della funzione di match dal rapporto segnale-rumore per studiare come varia l'efficienza di questo metodo di analisi in vari fondi di rumore. Questa simulazione permetterà di capire meglio l'efficienza di recupero dei segnali di onde gravitazionali negli interferometri della collaborazione LIGO-Virgo-Kagra.



# Contents

<b>Introduction</b>	<b>1</b>
<b>1 Gravitational Waves</b>	<b>3</b>
1.1 Gravitational waves in the weak field limit . . . . .	3
1.2 Optical Interferometers . . . . .	4
1.3 Compact binary coalescences . . . . .	5
1.4 Newtonian model . . . . .	5
<b>2 Newtonian chirps in a noise background</b>	<b>9</b>
2.1 Newtonian chirps . . . . .	9
2.2 Noise in the detectors . . . . .	10
2.3 Signal whitening . . . . .	12
2.4 Injection into Gaussian white noise background . . . . .	14
<b>3 Match vs. SNR</b>	<b>15</b>
3.1 Matched filters . . . . .	15
3.2 SNR . . . . .	16
3.3 Results . . . . .	17
<b>Conclusions</b>	<b>19</b>
<b>Appendix: Python code</b>	<b>21</b>
I Generating a Newtonian chirp . . . . .	21
II Waveform realization with PyCBC . . . . .	22
III Signal whitening and SNR calculation . . . . .	22
IV Calculating match . . . . .	23



# Introduction

The first detection of a Gravitational Wave (GW) signal on September 15th, 2014, marked a significant milestone and opened up a new world of exploration, providing a new method with which to investigate the cosmos. This was the culmination of decades of effort by a great scientific collaboration that have led to the development of a global network of highly sensitive detectors: today the relative distance between the mirrors in the interferometers can be measured with a spectral sensitivity better than  $10^{-23} \text{ m}/\sqrt{\text{Hz}}$  (as a comparison, the proton radius is about  $10^{-15} \text{ m}$ ) and work is underway to improve it further. However, this remarkable and unprecedented sensitivity comes at a cost: a significant amount of noise from various sources makes the detection of GWs an extremely challenging task. To overcome this challenge, scientists perform deep and complex data analysis, making good use of prior knowledge about the nature of astrophysical sources wherever possible. In some cases, the GW sources may also emit electromagnetic radiation and/or neutrinos, allowing multi-messenger observations of astrophysical phenomena. In such cases, real-time GW data analysis must be quite fast to provide an estimate of the position in the sky where the signal originated, and to quickly alert the astronomical community to look for an electromagnetic counterpart, for example. In this context, GW data analysis is an essential step to properly detect and interpret these signals.

The purpose of this thesis is to study some elements of GW data analysis, providing an analytical and numerical introduction to some important methods. The data analysis performed by the LIGO-Virgo-Kagra Collaboration is much more complex, involving refined statistical techniques as well as sophisticated parameterizations of Numerical Relativity results.

In this thesis, I synthesize GW signals, specifically chirps from the simple Newtonian model of compact binary coalescences (CBC), described in Chapter 1, and, in Chapter 2, I inject them into a Gaussian noise background. To understand chirp detection, in Chapter 3 I introduce the matched filtering technique. Matched filters are based on the overlap of a known signal template with a detected GW signal. The main result of this thesis is a study of the dependence of the *match function* on the Signal-to-Noise Ratio (SNR), which shows how the efficiency of this analysis method changes in different noise backgrounds.

When the signal model is known, matched filters are optimal linear filters that maximize the SNR in the presence of Gaussian white noise. Gaussianity is only approximate in the existing GW interferometers, mostly due to many types of transient instrumental artifacts, called glitches. Despite this, matched filters play a crucial role because they constitute the foundation of several analysis pipelines and the simulations, reported in Chapter 3, provide a better understanding of how and how much non-Gaussianities in the noise spectrum affect the GWs signal detection efficiency in the LIGO-Virgo-Kagra Collaboration interferometers.



# Chapter 1

## Gravitational Waves

In this chapter, I briefly review the theoretical background of General Relativity (GR), which is essential for understanding how gravitational waves arise in this theory and how we can detect them. Next, I will focus on GW emission in a compact binary coalescence (CBC), i.e., the merger of two compact objects, such as black holes or neutron stars, where the gradual spiral approach of the two objects (the *inspiral phase* of the coalescence) is due to the energy loss associated with the emission of GWs. Finally, I will describe the simple Newtonian model of the inspiral phase.

### 1.1 Gravitational waves in the weak field limit

The Einstein's field equations of GR are:

$$R_{\mu\nu} - \frac{1}{2} g_{\mu\nu} R = \frac{8\pi G}{c^4} T_{\mu\nu}. \quad (1.1)$$

These are non-linear differential tensorial<sup>1</sup> equations, where:

- $R_{\mu\nu}$  is Ricci's tensor, that is, a contraction of Riemann's tensor (curvature tensor),
- $g_{\mu\nu}$  is the metric tensor,
- $R$  is the Ricci scalar, that is, the trace of Ricci's tensor,
- $G$  is the universal gravitation constant and  $c$  is the light speed in vacuum,
- $T_{\mu\nu}$  is the energy-momentum tensor that describes the distribution of energy and matter everywhere in spacetime, and it represents the sources of gravitational field.

The *weak field limit* corresponds to the linear expansion of Einstein's field equation about the flat-space (Minkowski) metric, i.e.,  $g_{\mu\nu} = \eta_{\mu\nu} + h_{\mu\nu}$  where  $\eta_{\mu\nu}$  is the Minkowski tensor<sup>2</sup> and  $h_{\mu\nu}$  is the tensor that introduces a small curvature perturbation on flat space, with the assumption that  $|h_{\mu\nu}| \ll 1$ . Then, after expanding up to first order in  $h_{\mu\nu}$  the Ricci tensor and the Ricci scalar and introducing the reverse-trace metric as

$$\bar{h}_{\mu\nu} = h_{\mu\nu} - \frac{1}{2} \eta_{\mu\nu} h \quad \text{where} \quad h \equiv h^\sigma_\sigma, \quad (1.2)$$

leads to the linearized field equations, which can be expressed in Lorentz's gauge  $\partial_\nu \bar{h}^{\mu\nu} = 0$  as follows:

---

<sup>1</sup>Tensorial equations are covariant, which means that their form does not depend on the reference frame.

<sup>2</sup>The signature adopted here is  $(-, +, +, +)$ .

$$\square^2 \bar{h}_{\mu\nu} = -\frac{16\pi G}{c^4} T_{\mu\nu}. \quad (1.3)$$

Mathematically, this is a set of wave equations with source terms, and the situation is very similar to that occurring in classical electromagnetism. They describe the propagation in spacetime of the deviation from the flat-space metric,  $h_{\mu\nu}$ .

Linearized Einstein's field equations can be solved in vacuum, where  $\square^2 \bar{h}_{\mu\nu} = 0$ , and where they yield the usual wave-like solutions for each component of the  $h_{\mu\nu}$  tensor. These components are not all independent, because the Lorentz gauge still leaves some extra freedom. We determine them by imposing the conditions that the strain is transverse to the propagation direction and that  $h_{\mu\nu}$  is traceless (this is called the *Transverse-Traceless* or TT-gauge). In the TT-gauge the solution with a given wavevector  $k_\rho$  is a transverse plane wave:  $\bar{h}^{\mu\nu} = A^{\mu\nu} \exp(ik_\rho x^\rho)$ , where, since  $\bar{h}^{\mu\nu}$  is a symmetric tensor under index exchange, then so is the amplitude tensor  $A^{\mu\nu}$ . Moreover, the amplitude tensor  $A^{\mu\nu}$  has only two independent components:

$$A^{\mu\nu} = a e_+^{\mu\nu} + b e_\times^{\mu\nu}, \quad (1.4)$$

where  $a, b \in \mathbb{C}$ ,  $e_+^{\mu\nu}$  and  $e_\times^{\mu\nu}$  are respectively the *plus* and *cross* polarization tensors. In particular, these two linear polarization tensors form a basis and can be expressed as

$$[e_+^{\mu\nu}] = \begin{pmatrix} 0 & 0 & 0 & 0 \\ 0 & 1 & 0 & 0 \\ 0 & 0 & -1 & 0 \\ 0 & 0 & 0 & 0 \end{pmatrix} \quad [e_\times^{\mu\nu}] = \begin{pmatrix} 0 & 0 & 0 & 0 \\ 0 & 0 & 1 & 0 \\ 0 & 1 & 0 & 0 \\ 0 & 0 & 0 & 0 \end{pmatrix}. \quad (1.5)$$

Any possible polarization of a GW can be obtained by the linear superposition of these two tensors, and the generic expression of a GW with a given wavevector is

$$\bar{h}^{\mu\nu} = (h_+ e_+^{\mu\nu} + h_\times e_\times^{\mu\nu}) \exp(ik_\rho x^\rho) \quad \text{with} \quad h_+, h_\times \in \mathbb{C}. \quad (1.6)$$

## 1.2 Optical Interferometers

To detect GWs, scientists have developed different types of detectors, among which the most performing are undoubtedly the ground-based laser-interferometric detectors: they are modified Michelson interferometers and rely on the fact that the distance, and therefore the travel time of light, between two test masses – the interferometer mirrors – changes as the GW passes.

A simple interferometer scheme is shown in Figure 1.1: the detectors consist of two perpendicular arms with two mirrors suspended at their ends. Light from a laser is injected into the interferometer, and, through a beam splitter, half of it is reflected and goes into one arm, while the other half is transmitted and goes into the other. The light then travels in the resonant cavities of each arm and is reflected on the mirrors a very large number of times before the two beams from the two arms rejoin. The relative distance between the mirrors varies as GW passes through the interferometer. Therefore, when the two beams recombine, an interference pattern is observed, which is precisely the signal of a GW. The detectors actually measure the GW *strain*, a dimensionless quantity for the relative displacement between two test masses due to a passing GW. The sensitivity of existing interferometers is limited to the range from 10 Hz to  $10^4$  Hz, corresponding to astrophysical events such as the merging of stellar-mass black hole binaries and supernova explosions.

The first detection, on September 14th, 2015, of the GW signal named GW150914 <sup>3</sup>, was made by the two LIGO (Laser Interferometer Gravitational-Wave Observatory) interferometers in the United

---

<sup>3</sup>At that time, a GW event name was composed by the prefix “GW” plus the detection date in YY/MM/DD format.

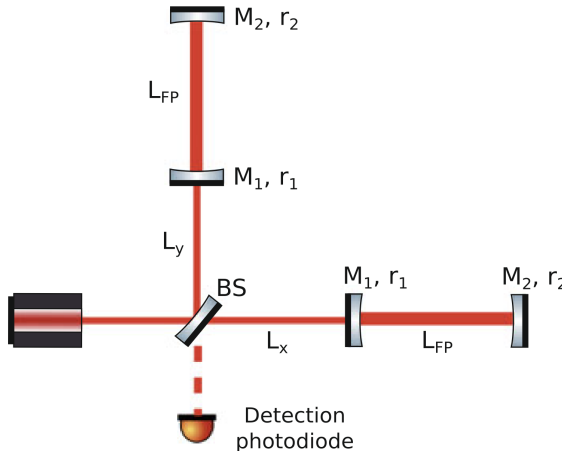


Figure 1.1: simplified scheme of a GW interferometer. The laser beam is split along the arms (respectively along the  $x$ -axis and  $y$ -axis of a Cartesian reference frame) by a beam splitter, then the light reaches the mirrors at the arms end (marked  $M_2$ ). After many reflections, the beam finally recombine and a photodiode collects it. The two pairs of dielectric mirrors  $M_1$  and  $M_2$  make up two Fabry-Perot resonant cavities that enhance the effect of the passing GWs.

States, during the first scientific observing run, named O1, which lasted from September, 2015, to January, 2016. The Virgo interferometer in Italy joined the network during the next observing run (O2, from November, 2016, to August, 2017). The Kagra interferometer in Japan joined the collaboration at the end of the second part of the O3b run (the O3 run is divided into O3a, from April, 2019, to September, 2019, and O3b, from November, 2019, to March, 2020). Figure 1.2 taken from [2] shows the detector outputs for GW150914, the first observed GWs signal.

### 1.3 Compact binary coalescences

Many astrophysical sources can emit GWs in different processes. The focus of my thesis is on CBCs, compact binary systems which comprise two compact bodies (such as two black holes, two neutron stars, or a black hole and a neutron star) that are orbiting around their center of mass. The system emits energy in the form of GWs at the expense of potential energy, and the two objects spiral toward each other, accelerating to higher and higher angular frequencies. The inspiral phase continues until the two bodies coalesce into a single object (merger phase), which then rings with oscillations dumped by the emission of GWs (ringdown phase). These main phases of the process are represented in Figure 1.3 from [8]: GWs from the inspiral and ringdown are well known respectively thanks to Post-Newtonian (PN) expansions and Perturbation Theory. At the same time, those emitted during a merger are more difficult to predict because of the strong relativistic regime, and are based on numerical solutions of Einstein's equations.

Here, I use PyCBC [13], an open-source pipeline for the analysis of GW signals from CBCs, to display a parameterized GW waveform. PyCBC interfaces to **LALsimulation**, a comprehensive package for GW simulations which is part of the **LIGO Algorithm Library** (LAL) [11], which includes many different parameterizations of CBC GW waveforms. In Figure 1.4, in blue, is displayed a waveform realized with PyCBC, corresponding to the GW150914 event (the actual code is in the Appendix, Section II). Between this waveform and the one in the second row of the Figure 1.2, there are several differences, however, both in shape and amplitude: in particular, in Figure 1.2 the waveform is modulated respectively by the response of the interferometers L1 and H1.

### 1.4 Newtonian model

In the Newtonian model for the CBCs, we assume that the conditions are those of the weak field and non-relativistic velocities, that the two objects are in a nearly circular orbit around the center of

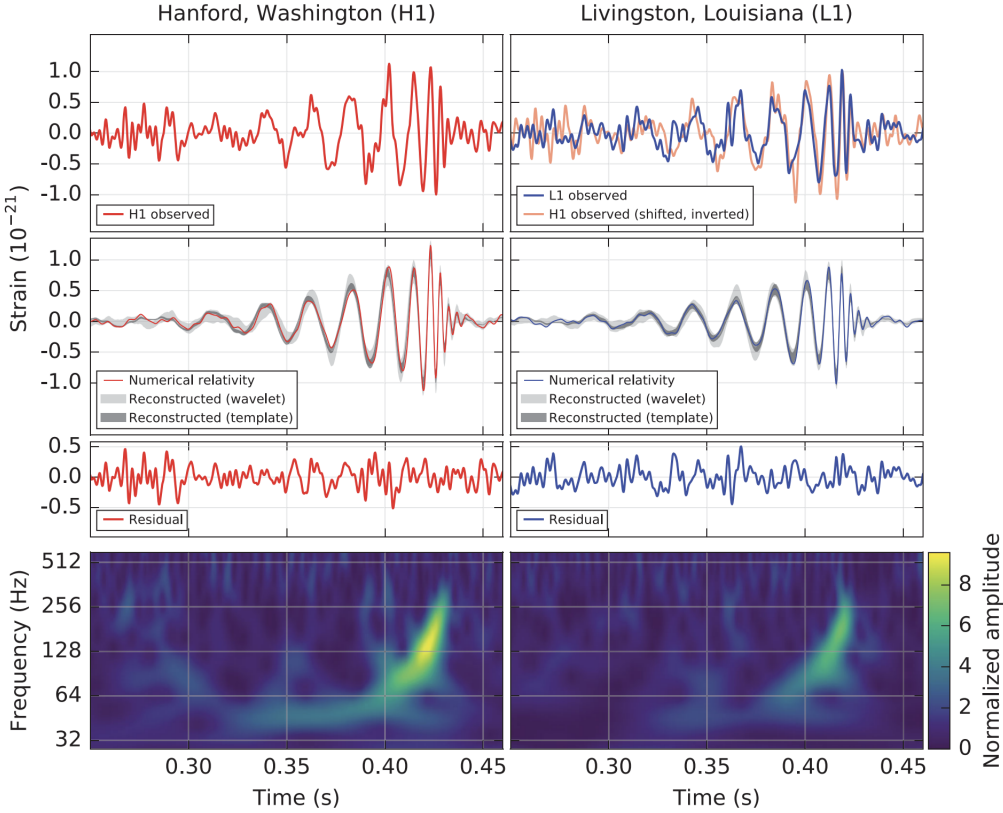


Figure 1.2: the first GWs event observed by the LIGO interferometers, H1 (Hanford, WA) and L1 (Livingston, LA). The first row shows the filtered and whitened strain (the whitening process will be explained in Chapter 2), and the second row shows the numerical relativity waveform and two types of waveform reconstruction from the data. In the third row, residuals between the filtered and whitened detector output and numerical relativity can be observed. At the bottom is the time-frequency representation of the strain data showing the *chirp*, the typical frequency increase over time in a CBC. The corresponding astrophysical event is the coalescence between two black holes that were about  $D = 440$  Mpc away from Earth: at the beginning, their masses (expressed in units of solar masses,  $M_\odot$ ) were respectively  $m_1 = 35.6 M_\odot$  and  $m_2 = 30.6 M_\odot$  and an energy equivalent to  $3M_\odot$  was radiated in the form of GWs during the process.

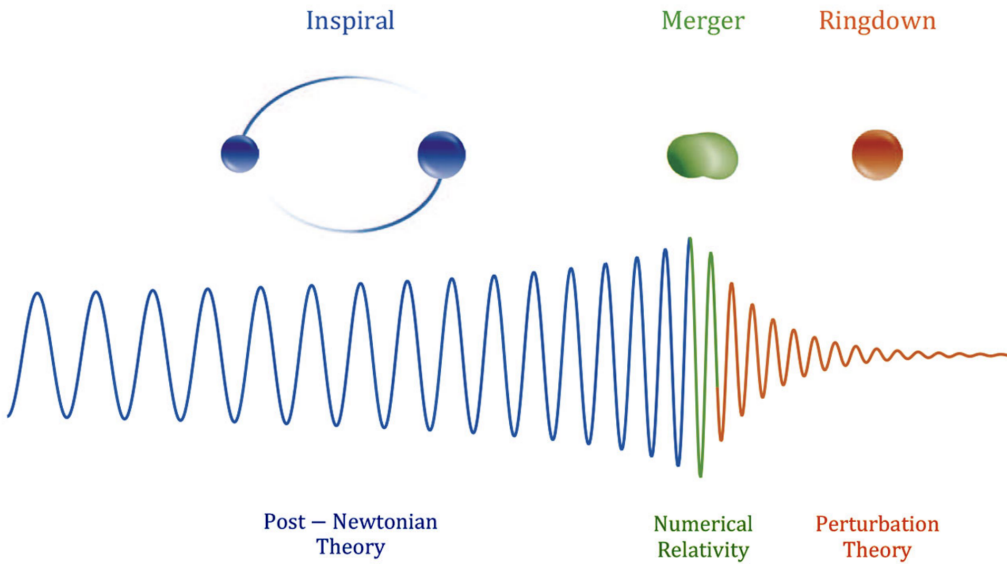


Figure 1.3: main phases of a CBC. At the bottom, there is the typical GW signal emitted by this type of coalescence, and at the top, there is a schematic representation of a CBC.

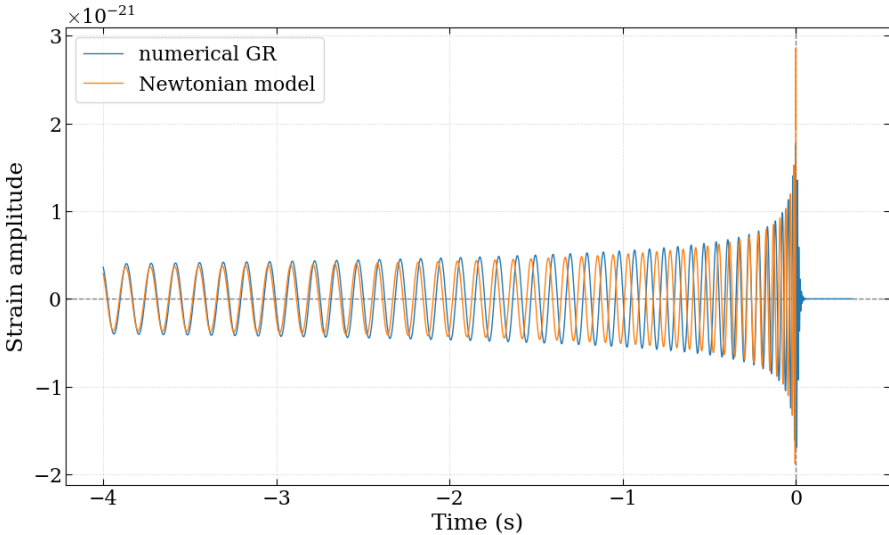


Figure 1.4: In blue, waveform obtained from EOBNRv2 model [14] in `LALSimulation` with plus polarization that fits the observed GW150914 GW signal. EOBNRv2 is an effective-one-body (EOB) model for waveforms emitted during a CBC of two non-spinning black holes, used also for the first GW detection. In orange, plus polarized strain with GW150914 parameters realized according to Newtonian model for CBC. Newtonian model for CBC is a reasonably good approximation almost up to coalescence, set at  $t = 0$  s. Phase at coalescence is set at  $\phi = 0$ .

mass, and that they have no spin. The model is a reasonable approximation far from the merger phase. The model has only two intrinsic parameters<sup>4</sup>, given by the masses  $m_1$  and  $m_2$  of the two component objects, and the frequency evolution of the chirp is mostly determined by just one parameter, the *chirp mass*, which will be described in detail later. It turns out that the Newtonian model is sufficient for a first understanding of CBC events [5, 12], and that it is possible to roughly estimate how far the system was from the Earth, its mass scale and the energy radiated via GWs.

It can be shown that in the Newtonian model, considering a non-relativistic compact binary system with circular orbits about the center of mass and composed of two objects respectively of masses  $m_1$  and  $m_2$  and orbital radii  $r_1$  and  $r_2$ , the strain in the TT-gauge for a GW propagating along the  $z$ -axis is

$$[\bar{h}^{\mu\nu}(ct, \vec{r})] = \frac{4c}{D} \left( \frac{GM_{\odot}}{c^3} \right)^{5/3} \frac{m_1 m_2}{(m_1 + m_2)^{1/3}} \omega^{2/3} \begin{pmatrix} \cos(2\omega t + \phi) & \sin(2\omega t + \phi) & 0 \\ \sin(2\omega t + \phi) & -\cos(2\omega t + \phi) & 0 \\ 0 & 0 & 0 \end{pmatrix}, \quad (1.7)$$

where  $D$  is the distance to the system,  $\omega$  is the angular frequency at which the system rotates (so  $\Omega = 2\omega$  is the pulsation of the emitted GWs) and  $\phi$  is the phase of the system at coalescence, and where  $m_1$  and  $m_2$  are expressed in units of solar masses.

A useful mass quantity to describe the GWs emission from a binary system is the *chirp mass*  $\mathcal{M}$ :

$$\mathcal{M} = \frac{(m_1 m_2)^{3/5}}{(m_1 + m_2)^{1/5}}. \quad (1.8)$$

The chirp mass  $\mathcal{M}$  is the main parameter determining the frequency evolution in the Newtonian model (Figure 1.5), with  $t_0$  the coalescence time,  $f_0$  as the maximum frequency in the merger and  $M = m_1 + m_2$  the total mass of the system:

<sup>4</sup>In general, the parameters that describe a CBC are either *intrinsic*, if they describe essential properties (masses and spins, 8 parameters in all), or *extrinsic*, if they describe incidental properties (distance, orbital inclination, sky location, coalescence phase and coalescence time, this is another 7 parameters)

$$f(t) = \left[ f_0^{-8/3} - \frac{256}{5} \pi^{8/3} \mathcal{M}^{5/3} \frac{G^{5/3}}{c^5} (t - t_0) \right]^{-3/8}, \quad (1.9)$$

$$f_0 = \frac{1}{2\pi\sqrt{2}} \left( \frac{GM_\odot}{c^3} \right)^{-1} \frac{1}{M/M_\odot}. \quad (1.10)$$

Using Equation 1.9, the time-frequency behavior of the observational data can be displayed (bottom row of Figure 1.2) and obtain the characteristic mass scale of the system, i.e., a rough estimate of the chirp mass  $\mathcal{M}$ .

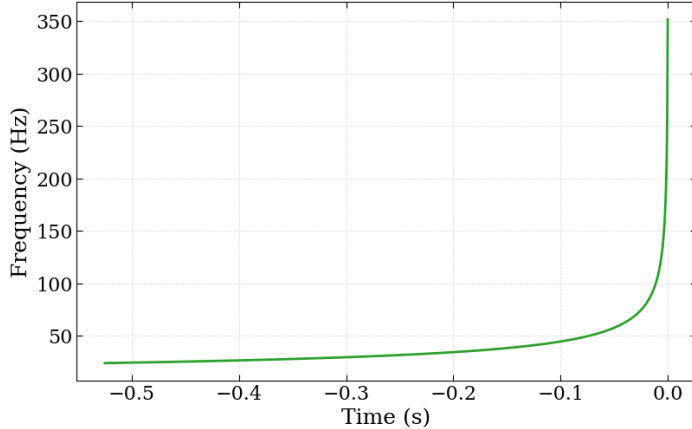


Figure 1.5: Newtonian approximation of the chirp using the GW150914 estimated parameters (Equation 1.9). The maximum frequency in the merger is about  $f_0 = 345$  Hz.

Finally, recalling that  $\Omega = 2\omega = 2\pi f$ , from Equation 1.7 and Equation 1.9, a GW signal with generic polarization results in:  $h(t) = h_+(t) + h_\times(t)$ , that is a linear combination of signals with only plus and cross polarization, respectively

$$h_+(t) = \frac{4c}{D} \left( \frac{GM_\odot}{c^3} \right)^{5/3} \frac{m_1 m_2}{(m_1 + m_2)^{1/3}} (\pi f)^{2/3} \cos(2\pi ft + \phi), \quad (1.11)$$

$$h_\times(t) = \frac{4c}{D} \left( \frac{GM_\odot}{c^3} \right)^{5/3} \frac{m_1 m_2}{(m_1 + m_2)^{1/3}} (\pi f)^{2/3} \sin(2\pi ft + \phi), \quad (1.12)$$

Finally, the phase at coalescence  $\phi$  is a free parameter in this model, and corresponds to the orbital phase at the coalescence time.

# Chapter 2

## Newtonian chirps in a noise background

In this chapter, I first present the reference signals that I will generate with the Newtonian model for CBCs and use them for the analysis. Next, an overview of how the interferometer responds to receiving a GW signal is fundamental to perform signal analysis. In this regard, I will briefly introduce the noise characteristics of the detectors that limit their sensitivity and signal detection, and how the detectors' sensitivity can be represented. Then I will present signal whitening, that is, filtering the synthesized chirps with the detector sensitivity function (the noise amplitude spectral density). Finally, I will inject the whitened signals into a Gaussian noise background, after analyzing its features.

### 2.1 Newtonian chirps

I have selected a list of GW events from [1], [6] and [7], and synthesized the corresponding chirps according to the Newtonian model for CBCs; selected events are presented in Table 2.1. These events correspond to CBCs, and their waveforms generated for subsequent analyses are as shown in Figure 1.4 with plus polarization (orange waveform).

Table 2.1: selected GW events list with their main features; events are presented chronologically. Event type is either a coalescence of two black holes (indicated with BH-BH) or between a black hole and a neutron star (indicated with BH-NS). For GW190814, there is uncertainty about its type because the estimated mass for the second component of the system points either to a heavy neutron star or a light black hole.

Event	Type	Run	$m_1 (M_\odot)$	$m_2 (M_\odot)$	$D (\text{Mpc})$
GW150914	BH-BH	O1	35.6	30.6	440
GW151226	BH-BH	O1	13.7	7.7	450
GW170104	BH-BH	O2	30.8	20	990
GW170608	BH-BH	O2	11	7.6	320
GW170814	BH-BH	O2	30.6	25.2	600
GW190412	BH-BH	O3a	30.1	8.3	740
GW190503_185404	BH-BH	O3a	43.3	28.4	1450
GW190521	BH-BH	O3a	95.3	69.2	3920
GW190814	BH-NS or BH-BH	O3a	23.2	2.59	240
GW190915_235702	BH-BH	O3a	35.3	24.4	1620
GW200105_162426	BH-NS	O3b	9	1.91	270
GW200115_042309	BH-NS	O3b	5.9	1.44	290

## 2.2 Noise in the detectors

In ground-based optical interferometers, such as LIGO and Virgo, GWs detection is hindered by a large amount of noise from various sources. Therefore, it is essential to study how noise affects detection, especially from a signal analysis point of view. The main noise sources are listed below, and their specific contribution depending on the frequency is shown in Figure 2.1 from [4]. These sensitivity curves show the detector's strain sensitivity at a given frequency. They summarize the noise budget for the LIGO detectors in the first scientific run (O1, the detectors' configuration was called *Advanced LIGO*). In the first two scientific runs, the strain sensitivities were similar between the two sites, Hanford and Livingston, and the first detection was made with such sensitivity. A noise budget is a quantitative analysis of the various sources of noise that affect the detectors' sensitivity: it is a critical tool for understanding a detector's performance and identifying potential sources of noise that may limit its sensitivity. The sensitivity of a detector is represented by the amplitude spectral density (ASD), the square root of the power spectral density (PSD).

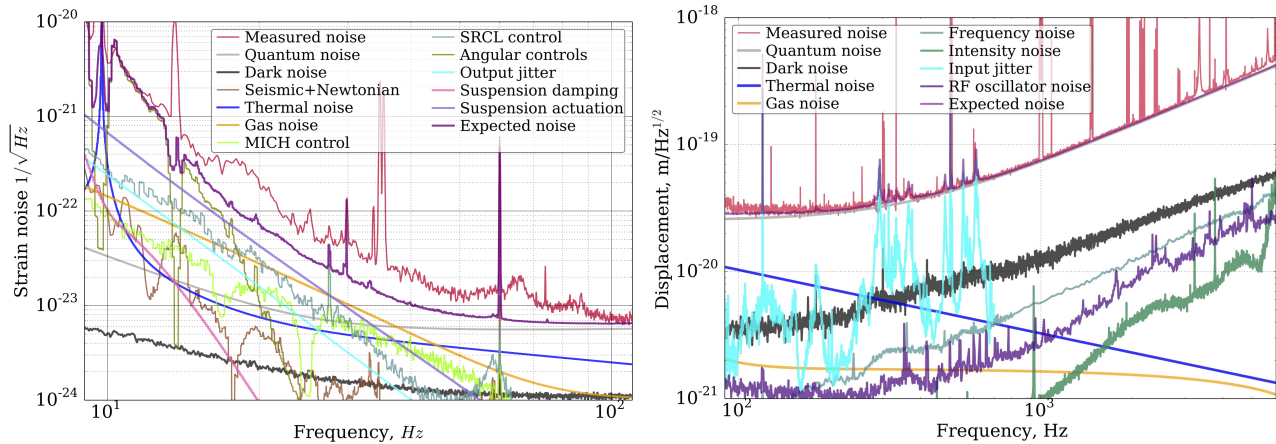


Figure 2.1: on the left, noise budget for L1 detector, from about 10 to 100 Hz (low-frequency curve). Dark noise refers to electronic noise in the signal chain with no light incident on the readout photodetectors. We notice a significant gap between the measured strain noise and the RMS sum of investigated noises (indicated with *Expected noise*). In particular, there is a significant peak around 60 Hz in the measured noise due to AC frequency in the US. On the right, the noise budget for the H1 detector ranges from about 100 to 1400 Hz (high-frequency curve). Here, the sensitivity is strongly limited by shot noise.

- **Quantum noise:** this is the sum of the quantum radiation pressure noise and the shot noise; these are fluctuations due to the quantum nature of light. Quantum radiation pressure is due to the high laser power because a fraction is transferred to the mirrors' mechanical modes, causing random fluctuations that degrade the sensitivity. Shot noise corresponds to the fluctuations in the number of photons reaching the photodiode, and it is related to the quantum, discrete nature of the photons. In Figure 2.1, on the right, it is clear that quantum noise places a lower limit on sensitivity in the frequency range between 100 and 1400 Hz.
- **Thermal noise:** this is the sum of the mirror suspension and the mirror coating thermal noises. Suspension thermal noise cause the test masses to move due to thermal vibrations of the suspension fibers. Thermal fluctuations of the optical coatings result in coating Brownian noise. Thermal noise significantly limits sensitivity at low frequencies, around 10 Hz.
- **Seismic noise:** it limits the sensitivity at low frequencies, below about 10 Hz, and it includes geological, seismic activity and anthropic activities. Seismic noise affects both mirrors and optical benches.
- **Newtonian noise:** it is a low-frequency noise associated with changes in the distribution of the masses surrounding the detector. As a consequence, there are gravitational gradients, not fully predictable and controllable, that act directly on the mirrors.
- **Gas noise:** due to the interactions of the residual gas particles in the cavities with the mirrors

and the laser light. Thermal motion of the gas molecules in the vacuum chambers results in momentum exchange with the mirrors via collisions; meanwhile, forward scattering of photons by the gas molecules in the arm vacuum pipes modulates the optical phase of the beam and results in sensing noise.

- **Charging noise:** residual charge distribution on cavities and mirrors that causes noise interactions.
- **Oscillator noise:** generated by radiofrequency modulation of laser light.
- **Laser amplitude and frequency noise:** this is due to laser intensity and frequency fluctuations.
- **Beam jitter:** minute fluctuations in the position and angle of the laser beam that can cause noise due to several optical effects.
- **Scattered light noise:** this noise is caused by minor imperfections in the mirrors that cause a fraction of the laser light to scatter toward the instrument's walls or other equipment. When this stray light mixes with the main beam, it can create a spurious signal in the readout photodetectors.
- **Electronic noise:** is generated by the analog and digital electronics used in signal detection and noise reduction systems.
- **Auxiliary degree-of-freedom noise:** due to the control of the position and alignment of the various mirrors in the detectors, together with the small mutual coupling between these mirrors.
- **Glitches<sup>1</sup>:** instrumental and environmental noise transients artifacts that hinder the search for transient GWs and whose precise cause is uncertain. They are non-Gaussian noise fluctuations that occur in many guises and can mask or mimic GW signals. Glitches occur frequently enough that they often can be coincident in the two detectors and can mimic astrophysical signals. They can be studied with spectral methods such as common spectrograms and *Omega Scans* (Figure 2.2).

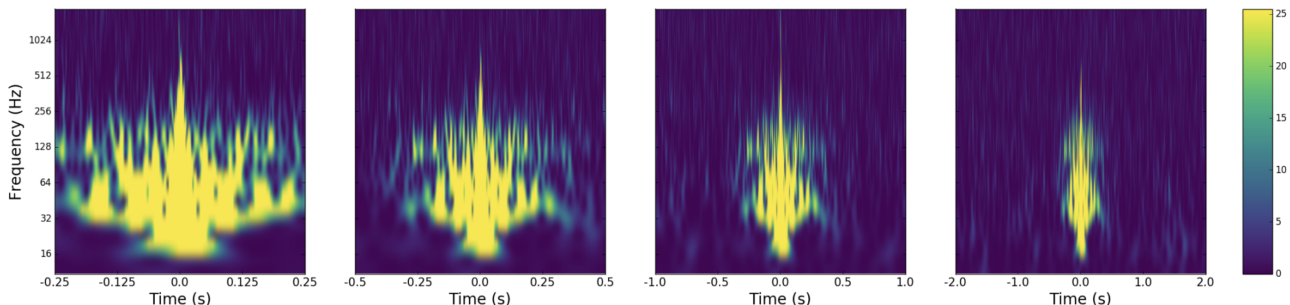


Figure 2.2: Omega scans that display a particular type of glitch, called *Koi-fish*, recorded in the H1 detector. Omega scans produce time-frequency maps at different temporal resolutions such as this one, using a multiresolution analysis method called *Q-transform* [10]. The amplitude corresponding to each time-frequency tile is indicated by the vertical color scale.

Finally, since the detectors are built on the Earth's surface, they are susceptible to transient weather conditions, especially variations in external temperatures and wind. In summary, the noise in the interferometers is far from being Gaussian and stationary over time.

Figure 2.3 shows the measured sensitivity curves of the LIGO and Virgo detectors during the first three months of the O3a run (the scientific run from April to June 2019)<sup>2</sup>. LIGO detectors' sensitivity significantly improved, and the peak around 60 Hz is smaller than in the first two observing runs. Virgo's sensitivity is not as good as that of the LIGO detectors mostly because the Advanced Virgo

---

<sup>1</sup>[9]

<sup>2</sup>[3]

project started later than Advanced LIGO and at this stage it does not include improvements like a more powerful laser and a signal recycling cavity.

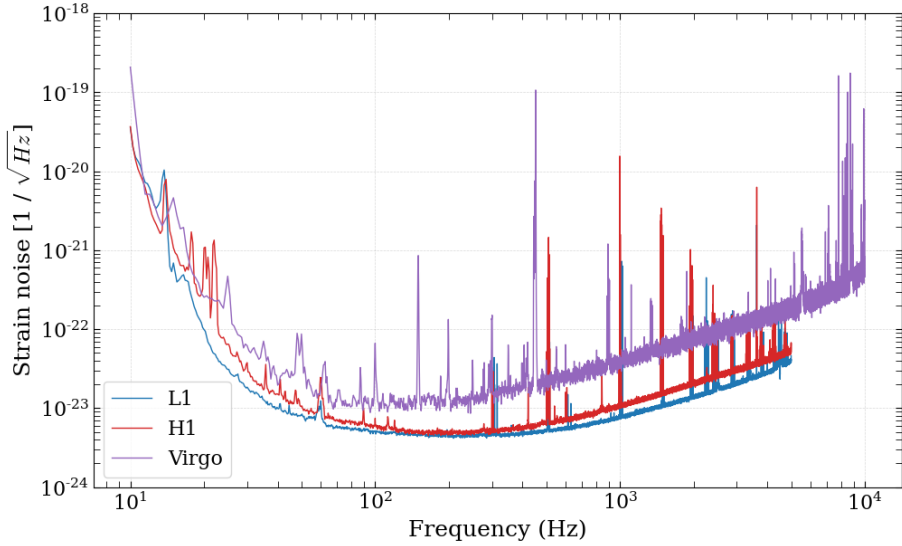


Figure 2.3: LIGO and Virgo detectors sensitivity, L1 in blue, H1 in red and Virgo in purple. The three curves reach their minimum between about 100 Hz and 300 Hz, where the detectors are most sensitive.

## 2.3 Signal whitening

The synthesized chirps must first be whitened: that is, the chirps must be filtered with the sensitivity curve of the interferometer. Here I used the sensitivity curve of the LIGO Livingston detector from O3a measurements (the blue curve in Figure 2.3).

First, I compute the Fourier transform of the signals. To perform this, I multiply each signal by a so-called *window function* to reduce the possible algorithmic artifacts that can prevent a proper analysis. This is due to the discontinuities of the signal at their extremes of the time domain: in the frequency domain, they produce non-physical artifacts. In practice, this is done with a one-sided tapered-cosine window far from the coalescence, and by setting the phase of the plus polarization  $\phi = 0$  (without lack of generality) to make the signal zero at the coalescence time. This procedure is shown in Figure 2.4, where the Newtonian  $h_+$  strain in Figure 1.4 is combined with the one-sided tapered cosine window.

Next, I compute safely the windowed Discrete Fourier Transform (DFT) of each signal. From this, I can compute, in order:

- 1) for each signal, the corresponding Power Spectral Density <sup>3</sup> (PSD, Figure 2.5);
- 2) the whitened signals' DFT by dividing the original DFT amplitude by the sensitivity curve;
- 3) the PSD of the whitened signals (Figure 2.6);
- 4) the SNRs of the signals (see Chapter 3);
- 5) finally, having obtained the DFT of the whitened signals, I perform an inverse DFT of the filtered signals getting the whitened signals in time domain.

<sup>3</sup>For a real signal in the time domain  $h(t)$ , the PSD is defined as it follows:

$$H(f) = \lim_{T \rightarrow \infty} \frac{2}{T} \left| \int_0^{\frac{T}{2}} h(t) e^{-2\pi i f t} dt \right|^2$$

which is a *single-sided spectral density* because for a real signal  $h(t)$ , it holds that  $H(f) = H(-f)$ . Also,  $T$  is the signal's duration.

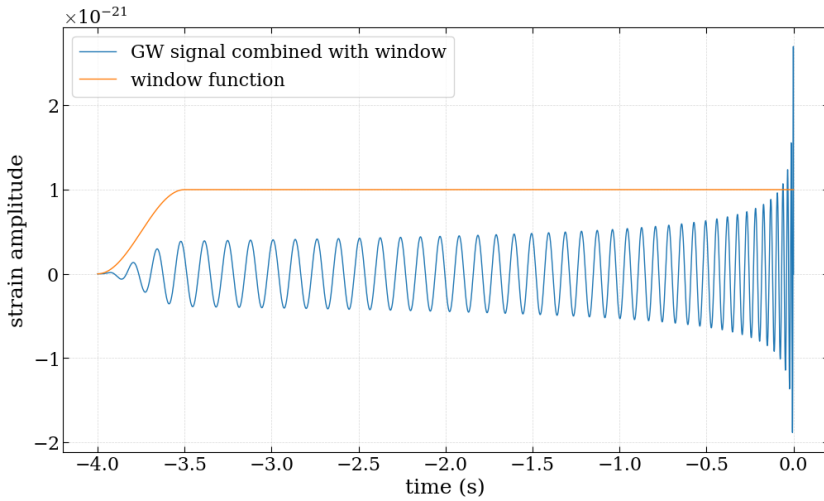


Figure 2.4: in blue signal with GW150914 parameters, plus polarization, combined with the window function *tapered cosine* (in orange, also called *Tukey window*), built in such a way as to bring the signal at its left end gradually to zero and leave it unchanged elsewhere. Window function amplitude is scaled for visualization purposes.

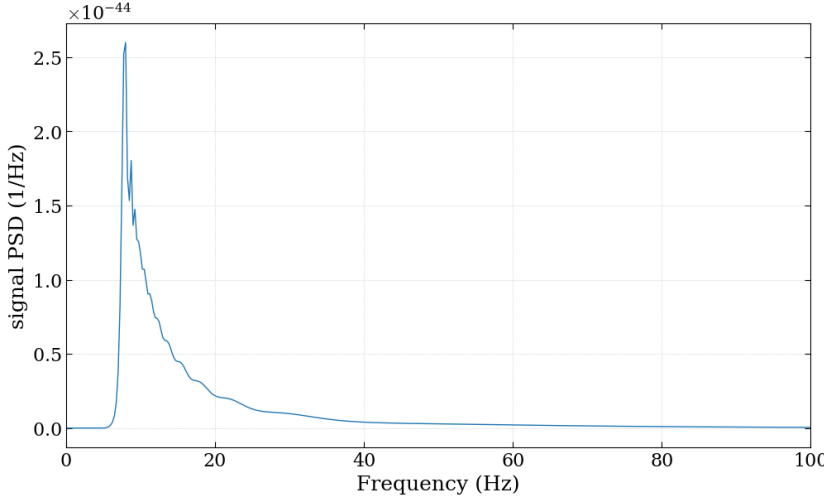


Figure 2.5: PSD of the signal with GW150914 parameters, plus polarization.

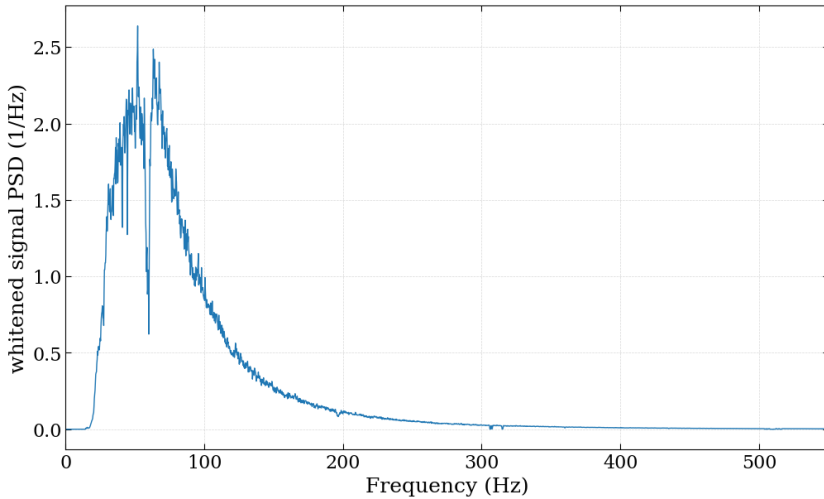


Figure 2.6: PSD of the whitened signal with GW150914 parameters, plus polarization.

In Figure 2.7, I present a whitened Newtonian chirp with the GW150914 parameters. Also from the comparison between Figure 2.5 and Figure 2.6, it is clear that the interferometer cuts the low-frequency components and enhances those in its maximum sensitivity range, and also adds spectral components not originally present.

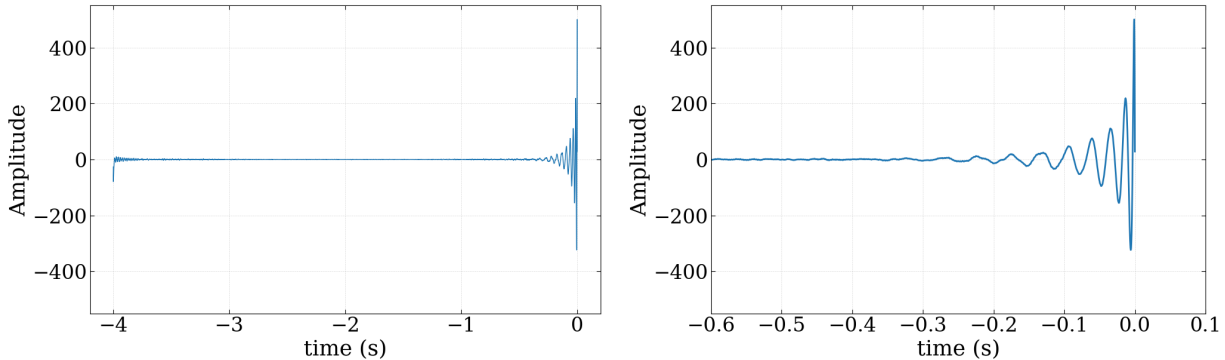


Figure 2.7: on the left, whitened signal with GW150914 parameters, plus polarization. There is an algorithmic artifact at the signal’s left end due to the discrete Fourier transform and its inverse; it does not affect the analysis. On the right, there is an insight into the whitened signal near coalescence.

## 2.4 Injection into Gaussian white noise background

I can complete the simulation of a whitened signal embedded in background noise by simulating a Gaussian white noise background in the time domain, as shown in Figure 2.8: its probability density function has a Gaussian distribution. Then I inject the whitened signals into this noise background. As explained above, this is not completely realistic, because the real noise background is not Gaussian, but it is a reasonable approximation to start with, and one that is suitable for the purpose of this thesis.

I repeat the injection into 100 different Gaussian white noise backgrounds and signal by signal. For each injection I compute SNR and match, as explained in Chapter 3, and use the repetitions to compute their statistical properties.

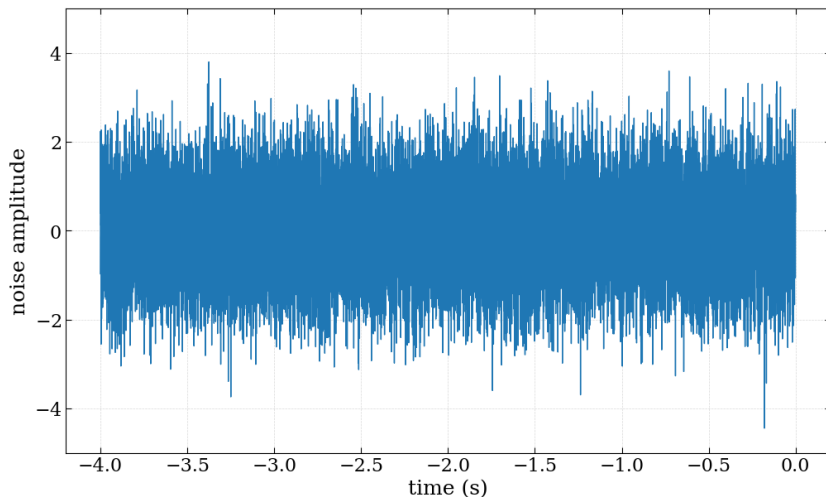


Figure 2.8: A single realization of a Gaussian white noise background; because of the whitening procedure, this stationary Gaussian noise has unit variance.

# Chapter 3

## Match vs. SNR

In this chapter, I introduce the matched filtering technique and I provide definitions for the *match function* and the Signal-to-Noise ratio. Finally, I present the result of the analysis of the match function as a function of SNR.

### 3.1 Matched filters

At the time of the first GWs detection, GW150914, the signal was confidently detected by two different types of searches [2]. One search targets a wide range of generic transient signals, with minimal assumptions about waveforms, while the other aims to recover signals from CBCs, using optimal matched filtering with waveforms predicted by GR. Indeed, matched filters are a fundamental tool for GWs data analysis.

It is possible to introduce matched filters using a Bayesian approach. Bayes theorem states that, for a null hypothesis  $\mathcal{H}_0$  and an alternative one  $\mathcal{H}_1$ , the posterior probability for  $\mathcal{H}_1$  hypothesis given the data  $s$  is

$$P(\mathcal{H}_1|s) = \frac{P(s|\mathcal{H}_1)P(\mathcal{H}_1)}{P(s|\mathcal{H}_0)P(\mathcal{H}_0) + P(s|\mathcal{H}_1)P(\mathcal{H}_1)}, \quad (3.1)$$

where  $P(s|\mathcal{H}_1)$  is called the likelihood function and  $P(\mathcal{H}_1)$  is the prior probability. The aim is then to select the hypothesis that maximize the posterior probability.

In GW data analysis, the data  $s(t)$  is given by the detector's output, i.e.,  $s(t) = h(t) + n(t)$ , where  $h(t)$  is a template signal (a *theoretically known* GW signal), and  $n(t)$  is the noise process. Thus, the null hypothesis in GW data analysis corresponds to the presence of pure noise,  $s(t) = n(t)$ . Meanwhile, the alternative hypothesis corresponds to the presence of a signal in addition to noise, i.e.,  $s(t) = h(t) + n(t)$ . In this simple case, with only two hypotheses and assuming a uniform prior for both, we only need to consider the *Bayes factor* to compare them:

$$\frac{P(\mathcal{H}_1|s)}{P(\mathcal{H}_0|s)} = \frac{P(s|\mathcal{H}_1)}{P(s|\mathcal{H}_0)}. \quad (3.2)$$

Equation 3.2 is precisely a likelihood ratio, i.e., the ratio between the two likelihood corresponding to  $\mathcal{H}_0$  and  $\mathcal{H}_1$ . Moreover, for a Gaussian noise process, it can be shown that the Bayes factor - the likelihood ratio - is given by the following expression:

$$\Lambda = \frac{P(s|\mathcal{H}_1)}{P(s|\mathcal{H}_0)} = \exp\left\{\frac{1}{2}\left[-\langle s(t) - h(t), s(t) - h(t) \rangle + \langle s(t), s(t) \rangle\right]\right\} = \quad (3.3)$$

$$= \exp\left\{\langle s(t), h(t) \rangle - \frac{1}{2}\langle h(t), h(t) \rangle\right\}, \quad (3.4)$$

which depends on data only through the scalar product  $\langle s(t), h(t) \rangle$ . Since the logarithm is a monotone function, instead of the likelihood ratio we can maximize its logarithm. This log-likelihood ratio is proportional to the scalar product  $\langle s(t), h(t) \rangle$ , which is defined in the frequency domain as

$$\langle s(t), h(t) \rangle = 4 \operatorname{Re} \int_0^{+\infty} \frac{\tilde{s}(f)\tilde{h}^*(f)}{S_n(f)} df, \quad (3.5)$$

using a single-sided noise spectral density  $S_n(f)$  as defined in Chapter 2, and with  $\tilde{s}(f)$  and  $\tilde{h}(f)$  the Fourier transform of  $s(t)$  and  $h(t)$ , respectively. Equation 3.5 defines the *matched filter*. Here, I wish to stress that the quantity  $\tilde{s}(f)/\sqrt{S_n(f)}$  is the Fourier transform of the whitened signal and  $\tilde{h}^*(f)/\sqrt{S_n(f)}$  is the whitened filter transfer function defined by the waveform template  $h(t)$  (or, equivalently, by a template  $\tilde{h}(f)$  in the frequency domain).

To apply the idea of matched filters to the detection of Newtonian signals in a noise background, I compute the *match function* in the time domain. It evaluates the match between a whitened template signal  $h(t)$  and the whitened template injected into a noise background in the time domain  $h_n(t)$ . The match function is defined as follows:

$$\text{match} = \frac{\langle h(t), h_n(t) \rangle}{\sqrt{\langle h(t), h(t) \rangle} \sqrt{\langle h_n(t), h_n(t) \rangle}}. \quad (3.6)$$

In this case the scalar product is defined in the time domain as

$$\langle h(t), h(t) \rangle = \sum_{k_{min}}^{k_{max}} h(k) h(k), \quad (3.7)$$

where  $k$  identifies a particular sample in time,  $k_{max}$  is the signal index corresponding to the time of coalescence and  $k_{min}$  is chosen such to exclude the left tail of the whitened signal:

$$\sum_{k_{min}}^{k_{max}} h(k) h(k) = 0.99 \times \sum_0^{k_{max}} h(k) h(k). \quad (3.8)$$

## 3.2 SNR

Ideally, the template signal  $h(t)$  is equal to the detected one  $s(t)$ . In this case, Equation 3.5, the expression defining the matched filters, becomes

$$\rho_{\text{opt}}^2 = 4 \int_0^{+\infty} \frac{|\tilde{h}(f)|^2}{S_n(f)} df \quad (3.9)$$

which is the *optimal power Signal-to-Noise ratio*, while its square root  $\rho_{\text{opt}}$  is the *optimal amplitude Signal-to-Noise ratio*. Comparing the equations defining the matched filter (Equation 3.5) and the match function (Equation 3.6), and the equation defining the signal to noise ratio (Equation 3.9), we expect a dependence of the match function on the SNR.

For each generated chirp, I calculate its optimal amplitude SNR, after filtering it with the interferometer sensitivity function. I remark here that this SNR depends on the many approximations and simplifications made in this work, and therefore differs from that computed with more accurate models in the LIGO-Virgo-KAGRA Collaboration papers – that is, the *network SNR*.

### 3.3 Results

To better understand how the match function depends on the optimal SNR, I selected a Newtonian chirp generated with GW150914 parameters and changed the source distance  $D$ , for a total of 8 chirps with modified distance, plus the original one. Modifying the distance does not take into account cosmological effects, such as the cosmological redshift (due to the expansion of the universe), but this is not important in the current context. For each one of these chirps, I compute the optimal amplitude SNR and estimate the mean match over 100 different Gaussian white noise backgrounds, with their associated standard deviation. Finally, I plot the mean match as in Figure 3.1. It is clear that as the SNR decreases, the match drops off abruptly after a certain value of SNR. When the SNR is very small, the match is close to zero: the signal is not found and the detection is not efficient.

As for the SNR value calculated for the signal obtained without changing the actual distance of GW150914 (the green circle in Figure 3.1), it is considerably higher than that corresponding to the actual detection, i.e.,  $\text{SNR} = 24$  (network SNR). This is mainly due to two reasons: the first is that the present calculation of the SNR refers to the sensitivity of the O3 run, which is much better than that of the first run when the first detection was made, so the SNR is consequently higher. Also, this simulation uses Gaussian noise, which is only an approximation of the interferometer noise, which has non-Gaussianities that cannot be predicted and are not constant over time (mainly due to glitches).

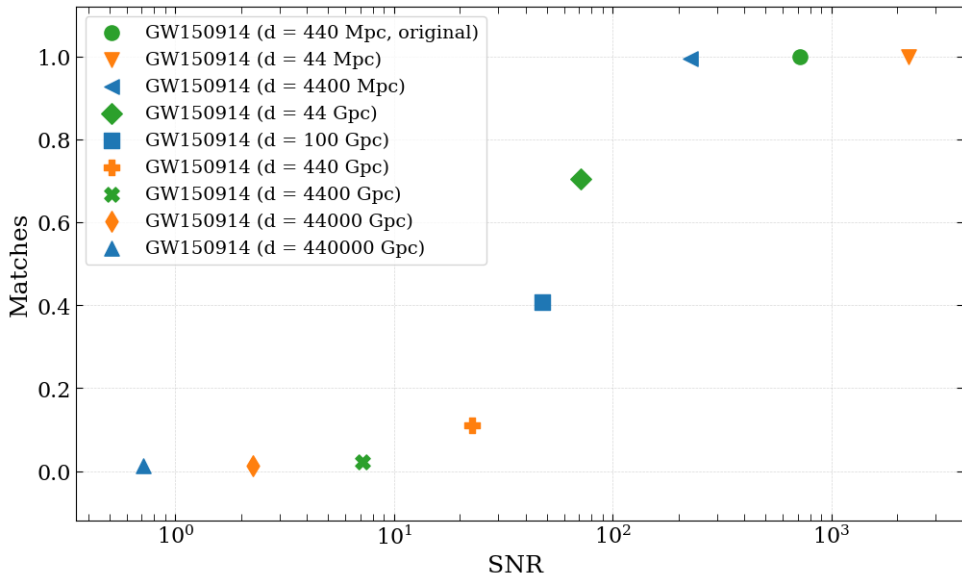


Figure 3.1: Mean match over 100 Gaussian white noise background realizations for each chirp as a function of the optimal amplitude SNR. The match samples have an approximately Gaussian distribution when the match is close to its maximum, however, when it decreases, the sample mean distributions are not well approximated by a Gaussian and are more scattered. Error bars are not shown because, in this simulation, the corresponding standard deviations are too small to be visualized: the first value (orange triangle) has a standard deviation in the range of  $10^{-9}$ , while the one corresponding to the last value (blue triangle) is in the range of  $10^{-3}$ .



# Conclusions

Gravitational waves are a very powerful tool for exploring the cosmos and its still-dark corners, as well as offering a testing ground for General Relativity and other theories of gravity. In this perspective, data analysis of GW signals is essential. In this thesis I explored the basics of data analysis of GW signals originating from CBCs: in particular, I used the Newtonian model of GW emission, which well approximates the GW strain during the early inspiral phase. I have generated a Newtonian chirp using the estimated astrophysical parameters of the first GW event ever detected, GW150914, and I have also compared it with a parameterized GR model that also covers the merger and ringdown phases.

Overall, the Newtonian model is sufficient to perform a basic signal analysis of the inspiral phase. I have generated several Newtonian chirps whose parameters correspond to CBC events that were actually detected. To analyze them, I have filtered them with the LIGO-Livingston sensitivity curve measured at the beginning of the O3a run. Then I injected each whitened chirp into a simulated Gaussian white noise background. The Gaussian noise is only an approximation of the noise actually present in the detectors, but it is suitable for the thesis' purpose.

To recover the chirps from the noise background, I have introduced matched filters, a detection technique that is based on searching for a known template signal in the detector output data. I have then evaluated the match function between the whitened signal (template) and the whitened signal injected into the noise background. For each signal, I calculated the match of over 100 different Gaussian white noise backgrounds and I have estimated the match mean and standard deviation of the match.

In addition, each GW signal has a different SNR depending on the parameters of the corresponding astrophysical event and the noise in the detectors. For each chirp I generated, I calculated its SNR, referring again to LIGO L1 sensitivity in O3a.

Since the match function depends on the SNR, I explored this dependence with a Newtonian chirp using the GW150914 parameters. By changing the distance parameter, I studied how the match decreases with decreasing SNR. The match function has a sigmoid shape and it reaches its saturation value when the SNR is above a certain threshold, while it decreases to zero when there is no match and the signal has not been found.

The main achievement of this thesis is the study of how the detection of the GW signal is performed, starting from the basic concepts of signal analysis to match filtering. In particular the study of the dependence of the match function on the SNR shows how and how much the noise background affects the detection with the matched-filter technique. This simulation is a simplification compared to the current one, where more complex models for astrophysical events and the resulting GW emission are considered, and the resulting analysis is deeper and mainly aims at estimating the astrophysical parameters of the source.



# Appendix: Python code

This section lists the most relevant parts of the Python code used to produce the results reported in this thesis.

## I Generating a Newtonian chirp

```
1 import numpy as np
2 import astropy.constants as const
3
4 # constants
5 G = const.G.value          # N m^2/kg^2
6 M_S = const.M_sun.value    # kg
7 C = const.c.value          # m/s
8
9 # time of coalescence (s)
10 t_0=0
11
12 # time
13 time_step = 1/(2*5000)
14 t = np.arange(-4,0,time_step)
15
16 # phase at coalescence (radian)
17 phi = np.pi/2
18
19 def chirp_mass_sm(m_1,m_2):
20     return pow(m_1*m_2,3/5)*pow(m_1+m_2,-1/5)
21
22 def chirp_mass(a,b):
23     return pow(a*b,3/5)*pow(a+b,-1/5)
24
25 def max_f(m_tot):
26     return pow(2*np.pi*np.sqrt(2),-1)*
27         pow(G*M_S/(pow(C,3)), -1)*M_S/m_tot
28
29 def frequency(f0,mc):
30     return pow(pow(f0,-8/3)-256/5*pow(np.pi,8/3)*pow(mc/M_S,5/3)*
31               pow((G*M_S)/pow(C,3),5/3)*(t-t_0),-3/8)
32
33 def a_factor(dist,m1sm,m2sm):
34     return 4*C/dist*pow(G*M_S,5/3)*pow(C,-5)*m1sm*m2sm*pow(m1sm+m2sm,-1/3)
35
36 def b_factor(freq):
37     return pow(np.pi*freq,2/3)
38
39 def strain(x,f):
40     return np.cos(2*np.pi*f*x+phi)
41
42 # GW150914 parameters
43 m1_sm = 35.6                  # compact object 1 mass (units of solar masses)
44 m2_sm = 30.6                  # compact object 2 mass (units of solar masses)
45 m1     = m1_sm*M_S             # compact object 1 mass (kg)
46 m2     = m2_sm*M_S             # compact object 2 mass (kg)
```

```

47     m      = m1+m2                      # total mass
48     d_pc   = 440*10**6                  # distance (pc)
49     d      = d_pc*3.086*10**(16)       # distance (m)
50
51     # chirp mass (solar masses)
52     mc_sm = chirp_mass_sm(m1_sm,m2_sm)
53     mc   = chirp_mass(m1,m2)
54
55     # maximum frequency in the merger (Hz)
56     f_0 = max_f(m)
57
58     # frequency
59     f = frequency(f_0,mc)
60
61     # strain with + (plus) polarization
62     h = a_factor(d,m1_sm,m2_sm)*b_factor(f)*strain(t,f)
63
64     # making sure is 0 for t = t_0 to avoid inaccuracies due to numerical accuracy
65     h[-1] = 0

```

## II Waveform realization with PyCBC

```

1  import numpy as np
2  import astropy.cosmology.parameters
3  import pycbc.waveform          #PyCBC package with various waveforms
4  # chirp parameter
5  m1 = 35.6        # solar masses
6  m2 = 30.6
7  d = 440          # Mp
8  # sampling time
9  dt = 10**(-4)

10 # waveform (plus and cross polarization)
11 hp, hc = pycbc.waveform.get_td_waveform(
12     approximant='EOBNRv2', # numerical model
13     mass1=m1, mass2=m2, distance=d, # parameters
14     f_lower=10, # starting frequency
15     delta_t=dt)

16 # time
17 t = np.linspace(-4,0.12,len(hp))
20

```

## III Signal whitening and SNR calculation

```

1  import numpy as np
2  import scipy.signal as signal
3
4
5  # import sensitivity data
6  L1_03 = np.loadtxt('L1_03.txt')
7  f_L3, s_L3 = L1_03.T # frequencies and sensitivity
8
9  # time
10 time_step = 1/(2*5000)
11 t = np.arange(-4, 0, time_step)
12 # window function
13 w = signal.windows.tukey(lenght, alpha=0.25, sym=True)
14 # cutting window right edge
15 w1 = np.where(t > -1, 1, w)
16 # combining signals with window
17 # where h is the strain calculated in the first section with GW150914 parameters
18 hw = h * w1

```

```

19 # discrete Fourier transform for a real signal
20 hf = fft.rfft(hw, norm="backward")
21 # corresponding frequencies
22 lenght = h.size()
23 delta_f = 1./(lenght * time_step)
24 f = delta_f * np.arange(0, lenght/2 + 1)
25 # modifying detector sensitivity array lenght
26 # to have the same lenght as sign
27 asd = np.concatenate((s_L3[0] * np.ones(40), s_L3))
28 # filtering signal
29 fil_sig = hf/asd
30 # calculating SNR
31 snr = np.sqrt(np.real(4*np.sum(np.conjugate(fil_sig)*fil_sig)*delta_f))
32 # inverse discrete Fourier transform
33 # to obtain whitened signal in time domain (for a real signal)
34 idft = fft.irfft(fil_sig, norm="backward")
35

```

## IV Calculating match

```

1 # excluding left tail of the whitened signal found in the previous section
2 idft1 = np.where(t>-0.4, idft, 0)
3
4 # norm
5 n = np.linalg.norm(idft1)
6
7 # excluding left tail of the whitened signal
8 # injected into Gaussian white noise background (hn)
9 hn1 = np.where(t>-0.4, hn, 0)
10
11 # norm
12 nn = np.linalg.norm(hn1)
13
14 # match
15 match = np.dot(idft1, hn1)/(n*nn)
16

```



# Bibliography

- [1] B. P. Abbott et al. “GWTC-1: A Gravitational-Wave Transient Catalog of Compact Binary Mergers Observed by LIGO and Virgo during the First and Second Observing Runs”. In: *Phys. Rev. X* 9.3 (2019), p. 031040. DOI: 10.1103/PhysRevX.9.031040. arXiv: 1811.12907 [astro-ph.HE].
- [2] B. P. Abbott et al. “Observation of Gravitational Waves from a Binary Black Hole Merger”. In: *Phys. Rev. Lett.* 116.6 (2016), p. 061102. DOI: 10.1103/PhysRevLett.116.061102. arXiv: 1602.03837 [gr-qc].
- [3] B. P. Abbott et al. “Prospects for observing and localizing gravitational-wave transients with Advanced LIGO, Advanced Virgo and KAGRA”. In: *Living Rev. Rel.* 21.1 (2018), p. 3. DOI: 10.1007/s41114-020-00026-9. arXiv: 1304.0670 [gr-qc].
- [4] Benjamin P. Abbott et al. “Sensitivity of the Advanced LIGO detectors at the beginning of gravitational wave astronomy”. In: *Phys. Rev. D* 93.11 (2016). [Addendum: Phys.Rev.D 97, 059901 (2018)], p. 112004. DOI: 10.1103/PhysRevD.93.112004. arXiv: 1604.00439 [astro-ph.IM].
- [5] Benjamin P. Abbott et al. “The basic physics of the binary black hole merger GW150914”. In: *Annalen Phys.* 529.1-2 (2017), p. 1600209. DOI: 10.1002/andp.201600209. arXiv: 1608.01940 [gr-qc].
- [6] R. Abbott et al. “GWTC-2: Compact Binary Coalescences Observed by LIGO and Virgo During the First Half of the Third Observing Run”. In: *Phys. Rev. X* 11 (2021), p. 021053. DOI: 10.1103/PhysRevX.11.021053. arXiv: 2010.14527 [gr-qc].
- [7] R. Abbott et al. “GWTC-3: Compact Binary Coalescences Observed by LIGO and Virgo During the Second Part of the Third Observing Run”. In: (Nov. 2021). arXiv: 2111.03606 [gr-qc].
- [8] Javier M. Antelis and Claudia Moreno. “Obtaining gravitational waves from inspiral binary systems using LIGO data”. In: *Eur. Phys. J. Plus* 132.1 (2017). [Erratum: Eur.Phys.J.Plus 132, 103 (2017)], p. 10. DOI: 10.1140/epjp/i2017-11283-5. arXiv: 1610.03567 [astro-ph.IM].
- [9] S. Bahaadini et al. “Machine learning for Gravity Spy: Glitch classification and dataset”. In: *Info. Sci.* 444 (2018), pp. 172–186. DOI: 10.1016/j.ins.2018.02.068.
- [10] S Chatterji et al. “Multiresolution techniques for the detection of gravitational-wave bursts”. In: *Classical and Quantum Gravity* 21.20 (Sept. 2004), S1809–S1818. DOI: 10.1088/0264-9381/21/20/024. URL: <https://doi.org/10.1088%2F0264-9381%2F21%2F20%2F024>.
- [11] LIGO Scientific Collaboration. *LIGO Algorithm Library - LALSuite*. free software (GPL). 2018. DOI: 10.7935/GT1W-FZ16.
- [12] Harsh Mathur, Katherine Brown, and Ashton Lowenstein. “An analysis of the LIGO discovery based on Introductory Physics”. In: *Am. J. Phys.* 85 (2017), p. 676. DOI: 10.1119/1.4985727. arXiv: 1609.09349 [gr-qc].
- [13] Alex Nitz et al. *gwastro/pycbc: v2.0.6 release of PyCBC*. Version v2.0.6. Jan. 2023. DOI: 10.5281/zenodo.7547919. URL: <https://doi.org/10.5281/zenodo.7547919>.
- [14] Yi Pan et al. “Inspiral-merger-ringdown multipolar waveforms of nonspinning black-hole binaries using the effective-one-body formalism”. In: *Physical Review D* 84.12 (Dec. 2011). DOI: 10.1103/physrevd.84.124052. URL: <https://doi.org/10.1103%2Fphysrevd.84.124052>.

